Spatiotemporal Hemodynamic Complexity in Carotid Arteries: An Integrated Computational Hemodynamics and Complex Networks-Based Approach

Spatiotemporal Hemodynamic Complexity in Carotid Arteries: an Integrated Computational Hemodynamics & Complex Networks-Based Approach

Karol Calò, Diego Gallo, David A. Steinman, Valentina Mazzi, Stefania Scarsoglio, Luca Ridolfi, and Umberto Morbiducci*

The final publication is available at: https://ieeexplore.ieee.org/document/8880534

***Abstract*— *Objective*: The study of the arterial hemodynamics is essential for a better understanding of the risks associated with the onset/progression of vascular disease. However, conventional quantification and visualization paradigms are not sufficient to fully capture the spatiotemporal evolution of correlated blood flow patterns and their "sphere of influence" in complex vascular geometries. In the attempt to bridge this knowledge gap, an integrated computational hemodynamics and complex networks-based approach is proposed to unveil organization principles of cardiovascular flows. *Methods*: The approach is applied to ten patient-specific hemodynamic models of carotid bifurcation, a vascular bed characterized by a complex hemodynamics and clinically-relevant disease. Correlation-based networks are built starting from time-histories of two fluid mechanics quantities of physiological significance, respectively (1) the blood velocity vector axial component locally aligned with the main flow direction, and (2) the kinetic helicity density. *Results*: Unlike conventional hemodynamic analyses, here the spatiotemporal similarity of dynamic intravascular flow structures is encoded in a distance function. In the case of the carotid bifurcation, this study measures for the first time to what extent flow similarity is disrupted by vascular geometric features. *Conclusion*: It emerges that a larger bifurcation expansion, a hallmark of vascular disease, significantly disrupts the network topological connections between axial flow structures, reducing also their anatomical persistence length. On the contrary, connections in helical flow patterns are overall less geometry-sensitive. *Significance*: The integrated approach proposed here, by exploiting the connections of hemodynamic patterns undergoing similar dynamical evolution, opens avenues for further comprehension of vascular physiopathology.**

***Index Terms*— Carotid bifurcation, complex networks, computational hemodynamics, helical flow, spatiotemporal analysis.**

I. Introduction

THE well-established role of hemodynamics in the onset and progression of vascular dysfunction, defining what is often referred to as the "hemodynamic risk" [1], makes the study of cardiovascular flows of wide interest. However, a full exploitation of the richness of information inherent to cardiovascular flows, made available by the adoption of in vivo four-dimensional (4D) flow MRI [2] and of personalized computational hemodynamics [3], poses several challenges. In fact, this large amount of hemodynamic data still needs for efficient methods distilling the arterial blood flow complexity in more intuitive, effective, and ultimately clinically relevant, hemodynamic quantifications and visualizations.

In this context, a variety of hemodynamic descriptors has been proposed to visualize and quantify those flow disturbances in relation with aggravating biological events. Historically, the firstly proposed description of flow disturbances was based on wall shear stress (WSS), as it represents the interaction between blood flow and the vessel wall [4], [5]. More recently, such information has been extended and integrated with descriptors for the quantitative analysis and visualization of intravascular flow patterns, motivated by the presumption that intravascular fluid structures elicit those fluid-wall interactions involved in the onset of vascular disease. In this regard, a physiological significance has been attributed to helical flow, a main feature of arterial hemodynamics, as it induces flow stability suppressing flow disturbances at the arterial wall [6]-[12].

Such intravascular flow features are typically represented through integrated quantities and/or through conventional visualization paradigms which, although intuitive, are only partially effective in capturing how blood flow patterns evolve and correlate in complex vascular geometries. Therefore, accurate knowledge on the spatiotemporal evolution of fluid structures and on their level of organization could be of paramount importance, supporting basic research on

K. Calò, D. Gallo, V. Mazzi, and U. Morbiducci* are with PolitoBIOMed Lab, Department of Mechanical and Aerospace Engineering, Politecnico di Torino, Turin, 10129 Italy. *(Correspondence e-mail:* umberto.morbiducci@polito.it.*)*

S. Scarsoglio is with Department of Mechanical and Aerospace Engineering, Politecnico di Torino, Turin, 10129 Italy.

D. A. Steinman is with Biomedical Simulation Lab, Department of Mechanical & Industrial Engineering, University of Toronto, Toronto, Ontario, ON M5S 3G8 Canada.

L. Ridolfi is with PolitoBIOMed Lab, Department of Environment, Land and Infrastructure Engineering, Politecnico di Torino, Turin, 10129 Italy.

cardiovascular flows and on the hemodynamic risk associated with vascular disease. Here we apply methods of the Complex Networks (CNs) theory to computational hemodynamics data, with the intent to uncover and highlight fundamental organization principles of the arterial hemodynamics.

The rationale for the use of CNs as tools of analysis lies in their ability to explore the structure and function of complex physical systems (i.e., 4D cardiovascular flows in our case) in a synthetic and effective manner.

Technically, CNs are based on graph theory and are used to model pairwise relations between interacting dynamical units [13], [14]. Besides the well-established applications to Internet, economy and social dynamics [15]-[17], CNs have been recently applied to fluid mechanics [13], [18], e.g., to study climate dynamics [19], [20], isotropic turbulence [21], [22], and turbulence in channel flows [23], [24]. In those contexts, the study of CNs topology has revealed information embedded in the time series of fluid dynamics quantities involved in nonlinear phenomena that theoretical models are unable to describe. Here, pairwise linear correlation between the time series of hemodynamic quantities is used to build CNs measuring their spatiotemporal similarity.

In this exploratory study, CNs are applied to the carotid bifurcation (CB), selected because of its intricate hemodynamics and its preferential atherosclerosis development. In detail, CNs ability in detecting the underlying hemodynamic features and organization is tested in a dataset of ten patient-specific computational fluid dynamics (CFD) models of human CB. Quantitative metrics derived from CNs theory are applied to the time-histories (along the cardiac cycle) of two fluid mechanics quantities describing the intricate intravascular hemodynamics: (1) the axial velocity, i.e. the blood velocity component aligned with the main flow direction; (2) the kinetic helicity density, a measure of pitch and torsion of the streaming blood [1]. These quantities were selected as they were previously shown to correlate with atherosclerotic biomarkers in the CB [25], [26]. The findings of this study highlight the potential of CNs in providing new pictures of the intravascular flows through the determination of the spatial scales of correlated hemodynamic structures and of their "persistence length" inside the CB.

II. METHODS

Data from this study are a subset of the Vascular Aging – The Link That Bridges Age to Atherosclerosis (VALIDATE) study. An overview of the methods applied in this study is provided in Fig. 1.

A. Computational Hemodynamics

The CB's geometry and flow rates at inflow and outflow sections of ten ostensibly healthy participants were acquired from contrast-enhanced angiography (CEMRA) and phase-contrast MRI (PC-MRI), respectively. The ten models were selected from the original VALIDATE dataset of 42 participants to represent the large inter-individual variability in flow disturbances [25]. As detailed in a previous study [27], the common carotid artery (CCA) lumen geometry was reconstructed from the thoracic segment, where possible, to above the bifurcation, using the open-source Vascular Modelling Toolkit (VMTK, www.vmtk.org).

Then, ICEM-CFD (ANSYS Inc., Canonsburg, PA) was used to generate uniform quadratic tetrahedral-element meshes. Details on the adopted numerical settings and schemes are exhaustively reported in a previous study [27]. The availability of PC-MRI measurements ensured patient-specific boundary conditions, as

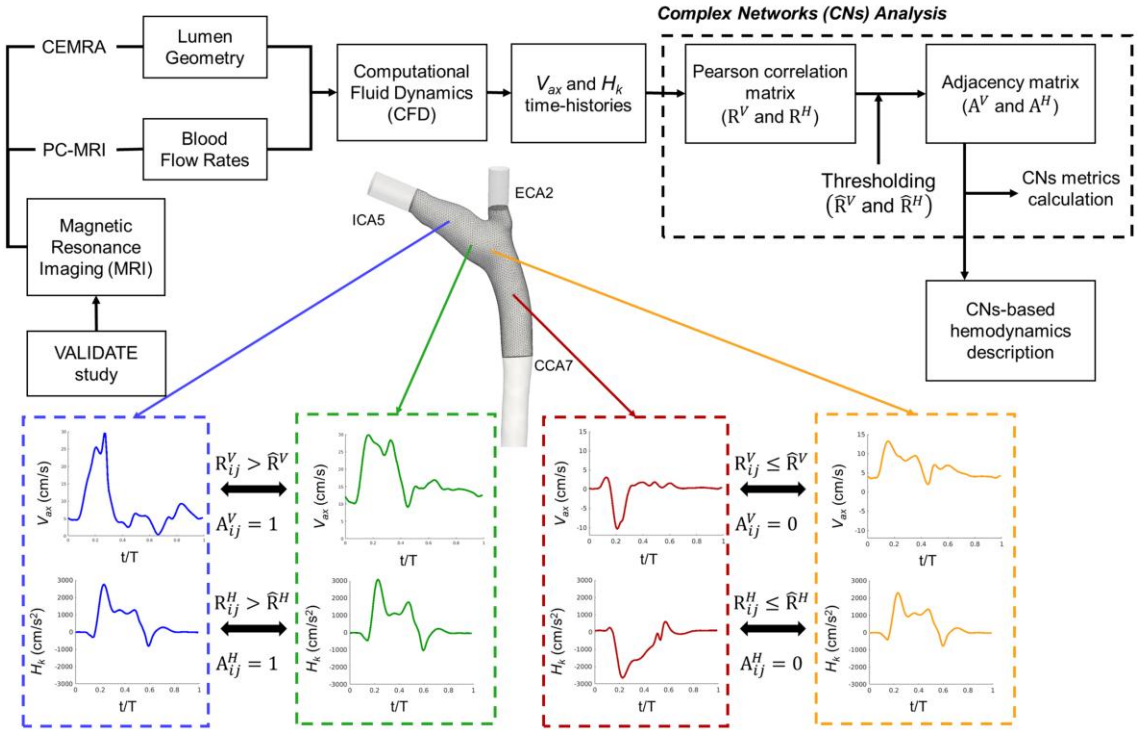

Fig. 1. Schematic diagram of the integrated computational hemodynamics and CNs-based approach. T: cardiac cycle duration; PC-MRI: phase-contrast MRI; CEMRA: contrast-enhanced magnetic resonance angiography.

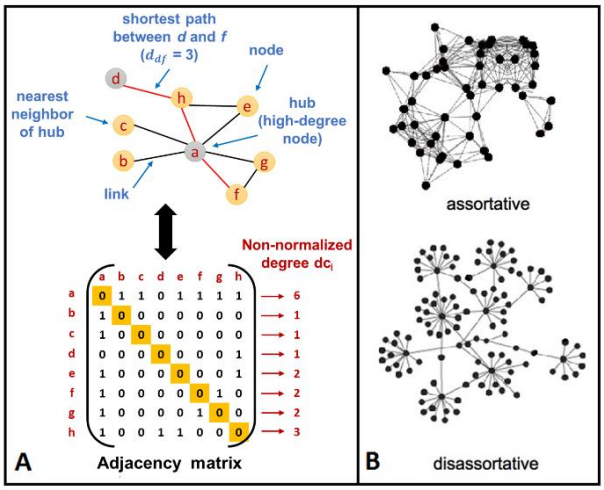

Fig. 2. Explanatory example of: A) a CN with its nodes and links, and the corresponding adjacency matrix; B) topological structures of assortative and disassortative CNs.

detailed elsewhere [25], [27]. To ensure fully-developed velocity profiles at the CCA inlet and to minimize the influence from outlet boundary conditions, flow extensions were added to the inlet and outlet faces of all CFD models. CFD simulations were carried out using a previously validated finite element-based in-house solver [28]. After CFD, using VMTK [29] all simulated models were truncated normal to the branch axis at locations 7, 2 and 5 radii of the local maximally inscribed spheres away from the branch division [9], [30] respectively for CCA, external (ECA) and internal (ICA) carotid artery (CCA7, ECA2 and ICA5 sections in Fig. 1, respectively), in order to ensure a consistent spatial extent across all cases for the CNs analysis [6], [27]. Each carotid geometry was characterized in terms of the expansion at the carotid bulb with respect to the CCA by the geometric descriptor *FlareA* (Fig. 14 in the Appendix). According to a previous study [31], *FlareA* was defined as the ratio between the maximum cross-sectional area at the CCA branch proximal to the flow divider and the CCA area at 3 maximally inscribed spheres radii upstream of the branch division (CCA3). Physically, a large expansion at the bifurcation with respect to the CCA promotes flow separation and in general flow disturbances in the bifurcation.

B. Intravascular Flow

Two fluid mechanics quantities, axial velocity (V_{ax}) and kinetic helicity density (H_k), were considered to describe the laminar intravascular flow in the CB, and CNs were applied to their time-histories along the cardiac cycle (Fig. 1). In detail V_{ax}, the axial component of blood velocity vector, representative of the main flow direction, was calculated by projecting the velocity vector field along the local vessel centerlines (i.e., the local axial direction, Fig. 15 in the Appendix), according to a scheme proposed elsewhere [32].

Based on the established physiological significance of arterial helical flow [8], [33]-[36], in particular in the CB [6], [9], [25], and on the recognized role of helicity in the evolution and stability of both turbulent and laminar flows [37], also in the context of hemodynamic flows [11], [12], intravascular blood flow patterns were also characterized using the kinetic helicity density H_k, defined as:

$$H_k(\mathbf{x},t) = \mathbf{V}(\mathbf{x},t)\cdot\boldsymbol{\omega}(\mathbf{x},t) \quad (1)$$

where $\mathbf{V}(\mathbf{x},t)$ and $\boldsymbol{\omega}(\mathbf{x},t)$ are the velocity and vorticity vectors, respectively. H_k is a pseudoscalar, i.e., roughly speaking its sign is an indicator of the (right- or left-handed) direction of rotation of helical blood flow patterns. To visualize helical blood flow patterns inside the bifurcation, here the local normalized helicity (LNH) [34] was adopted, defined as:

$$\mathrm{LNH}(\mathbf{x},t) = \frac{\mathbf{V}(\mathbf{x},t)\cdot\boldsymbol{\omega}(\mathbf{x},t)}{|\mathbf{V}(\mathbf{x},t)||\boldsymbol{\omega}(\mathbf{x},t)|}, \quad -1 \le \mathrm{LNH} \le 1. \quad (2)$$

If LNH is positive (negative), the helical flow structures are right- (left-) handed, i.e. their rotation is clockwise (counter-clockwise) when viewed in the direction of the forward movement.

C. Complex Networks: definition and construction

In graph theory, a CN is a network with markedly intricate patterns of connection between its elements and nontrivial topological features (an explanatory example is presented in Fig. 2). In detail, a network is defined by a set V of N of nodes and a set E of links $\{i, j\}$. Here we deal with *spatial networks*, i.e., networks with nodes occupying a precise position in the Euclidean space, here represented by the grid points of the finite element mesh used to perform CFD simulations. In the class of spatial networks considered in this study only one link is admitted between each pair of nodes and no self-loops $\{i, i\}$ are allowed.

For each CB model, *"all-to-all"* CNs were built from V_{ax} and H_k time-histories, respectively, by applying a correlation criterion. Technically, for each pair of nodes $\{i, j\}$ of the discretized fluid domain, the linear Pearson correlation coefficient R_{ij} was calculated between the time-histories (along the cardiac cycle) of V_{ax} or of H_k at nodes i and j. For both V_{ax} and H_k quantities, a correlation matrix containing the R_{ij} coefficients was created, and the corresponding network was built up based upon the constraint that a topological link between nodes i and j exists if and only if R_{ij} is greater than a threshold $\widehat{\mathrm{R}}$ (Fig. 1). The nontrivial aspect of properly setting the threshold value $\widehat{\mathrm{R}}$ [19], [20], [22], [38], was here addressed as follows: both for the V_{ax}- and the H_k-based networks the overall distribution obtained by pooling together the respective R_{ij} correlation coefficients of all ten CB models was considered. For the V_{ax}-based networks, the median value of the R_{ij} correlation coefficients distribution was set as threshold value ($\widehat{\mathrm{R}}^V = 0.506$). For the H_k-based networks, the correlation threshold was set equal to $\widehat{\mathrm{R}}^H = 0.000$. The threshold value $\widehat{\mathrm{R}}^H$ was selected because of its physical meaning, since it allows to separate helical flow structures according to their direction of rotation (as opposite signed values of quantity H_k are expected to yield negative correlation coefficients). Notably, the set threshold value $\widehat{\mathrm{R}}^H = 0.000$ for the H_k-based networks is very close to the median value of the R_{ij} correlation coefficients distribution, which is equal to 0.006. Explanatory examples of pairs of V_{ax} and of H_k nodal time-histories with different correlation strength and sign (as defined by R_{ij} values) are presented in Fig. 3.

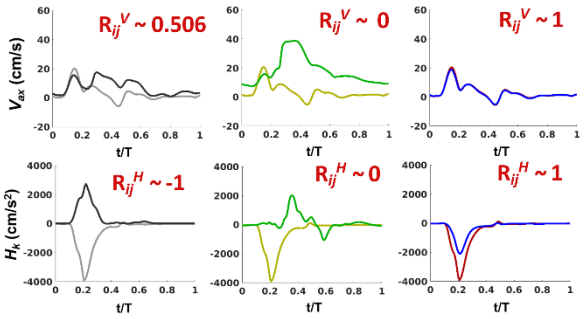

Fig. 3. Explanatory examples of differently correlated pairs of V_{ax} and H_k time-histories along the cardiac cycle of duration T, as defined by the R_{ij} correlation coefficients.

Based on R_{ij} and $\hat{R}$ values, an *adjacency matrix* can be built up for each *"all-to-all"* CN as follows (Fig. 2):

$$A_{ij} = \begin{cases} 0, \ if \ \{i,j\} \notin E \ or \ \ i = j, \\ 1, \ if \ \{i,j\} \in E \end{cases} \quad (3)$$

where E is the set of the CN links. Matrix A contains all the information about node connectivity. More in detail, A_{ij}=1 if a link exists between nodes *i* and *j* (i.e., if $R_{ij}>\hat{R}$), and is equal to zero otherwise. The steps followed in this study to construct undirected ($A_{ij}=A_{ji}$) CNs are presented in Fig. 1.

A *"one-to-all"* approach was also applied to investigate the relationship between the shape of V_{ax} time-histories in the CB and the patient-specific, measured CCA flow rate waveform shape. To do so, for each CB model the Pearson correlation coefficient R_i^Q was calculated between the V_{ax} time-history at each node *i* of the discretized fluid domain and the personalized volume flow rate time-history Q used as inflow boundary condition in the numerical simulation.

D. Complex Networks Metrics

In this study topological CNs metrics (the meaning of some of them is anticipated in Table I) were calculated to characterize the structure of the *"all-to-all"* and *"one-to-all"* networks.

A measure of the centrality of a node *i* is the *degree centrality* (DC_i), defined as the percentage of nodes of the network directly connected to node *i*, i.e., the so-called *nearest neighborhood* of *i*. Here we consider DC_i normalized over the total number $(N-1)$ of possible neighbors of *i*:

$$DC_i = 100\left(\frac{1}{(N-1)}\sum_{j=1}^{N} A_{ij}\right) = 100\left(\frac{1}{(N-1)} dc_i\right), \quad (4)$$

where dc_i is the non-normalized degree centrality of node *i*. The normalization introduced in (4) allows comparisons between networks of different number of nodes (N). In synthesis, the DC_i is a measure of the fraction of the total CB volume connected to node *i*.

Correlations between the degrees of neighbor nodes inside a network can be evaluated by calculating the *average nearest neighbors normalized degree centrality* of node *i* [13], defined as:

$$DC_{nn,i} = 100\left(\frac{1}{DC_i(N-1)}\sum_{j\in n(i)} DC_j\right), \quad (5)$$

where the sum runs over *n(i)*, i.e., the set of the nearest neighbors of node *i*. By using the definition (5), the average degree of centrality of nearest neighbors for nodes of degree centrality DC, denoted as $\langle DC_{nn}|DC\rangle$, can be calculated, obtaining an expression that implicitly incorporates the dependence on DC. Previous studies have classified networks as "assortative" if $\langle DC_{nn}|DC\rangle$ is an increasing function of DC, whereas they are referred to as "disassortative" when $\langle DC_{nn}|DC\rangle$ is a decreasing function of DC [39]. In other words, in assortative networks the nodes tend to connect to their connectivity peers, while in disassortative networks nodes scarcely connected are more likely connected with highly connected nodes, and vice versa (Fig. 2). Assortativity of a network can be quantified by calculating the Pearson correlation coefficient between DC values at the two ends of each link, namely the *assortativity coefficient* r, that for an undirected network can be defined as [39]:

$$r = \frac{M^{-1}\sum_{k=1}^{M} DC_k^- DC_k^+ - [M^{-1}\sum_{k=1}^{M}\frac{1}{2}(DC_k^- + DC_k^+)]^2}{M^{-1}\sum_{k=1}^{M}\frac{1}{2}([(DC_k^-)^2 + (DC_k^+)^2]) - [M^{-1}\sum_{k=1}^{M}\frac{1}{2}(DC_k^- + DC_k^+)]^2} \quad (6)$$

where DC_k^- and DC_k^+ are the DC values of the nodes at the ends of the *kth* link, with k = 1,.., M. Note that (6) is written in a form manifestly symmetrical in DC_k^- and DC_k^+, so that it does not matter which is the initial or ending node of the generic link, since in an undirected network the links have no orientation. Based on (6), if r>0, the network is assortative, disassortative if the opposite holds.

A measure of the topological distance between couples of nodes $\{i,j\}$ in the network, is given by the *average shortest path length* $ASPL$ of the network:

$$ASPL = \frac{1}{N(N-1)}\sum_{i,j\in N, i\neq j} d_{ij}. \quad (7)$$

$ASPL$ is defined as the mean of the *shortest path lengths*, where $d_{ij} \in \mathbb{Z}$ is the shortest topological distance between nodes *i* and *j*, i.e., the minimum number of links that have to be crossed from node *i* to node *j* [13] (Fig. 2).

Finally, in order to provide a quantitative measure of the anatomical "persistence length" of correlation of axial velocity and helical flow structures inside the CB, we calculated the normalized *average Euclidean distance* (AED_i) [22] of each node *i* of the network from all its nearest neighbors *n(i)*, defined as:

$$AED_i = \frac{1}{dCCA7}\frac{\sum_{j\in n(i)} l_{ij}}{dc_i} \quad (8)$$

where $dCCA7$ is the CCA7 diameter of the specific CB model, and l_{ij} is the Euclidean distance between neighbor nodes *i* and *j*. The definition of AED_i in (8) allows an effective quantification and visualization of "the sphere of influence" of local hemodynamic patterns inside the vascular domain, and their main direction of propagation: high AED_i values indicate a large anatomical distance (expressed in terms of CCA7 diameters) between node *i* and its nearest neighbors, while low AED_i values indicate that all the nodes directly connected to node *i* are physically located close to it. According to this, intravascular fluid structures characterized by high AED keep their correlation within a large spatial distance, while for structures having low AED, their correlation vanishes within a shorter distance.

The quantitative analysis of the *"one-to-all"* network was carried out using an ad-hoc defined metric, as follows: (1) for

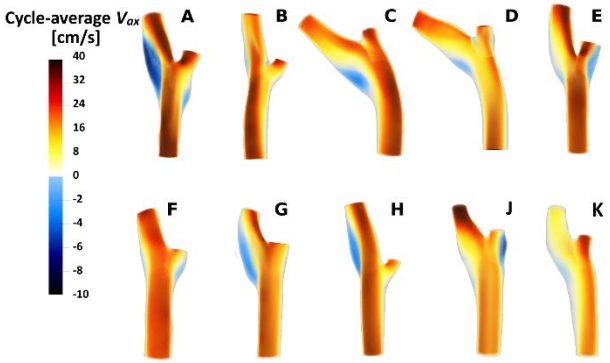

Fig. 4. Volumetric maps of the cycle-average axial velocity V_{ax} in the ten CB models. Negative values in the map indicate the presence of flow reversal.

all the nodes in the CB the anatomical distance from the CCA7 center of mass (Fig. 1) was calculated and denoted as l_{i-CCA7}; i = 1,…N; (2) then, the Euclidean distances l_{i-CCA7} from CCA7 were weighted by the value of the correlation coefficient, R_i^Q, between V_{ax} at node i and the subject-specific flow rate Q at the inlet, to obtain the *average weighted Euclidean distance* ($AWED$):

$$AWED = \frac{1}{dCCA7}\frac{\sum_{i=1}^{N} l_{i-CCA7}\mathrm{R}_i^Q}{N}. \quad (9)$$

Because of the well-known high inter-individual geometric variability observed in the CB [6], in this study the values of the AED and $AWED$ were normalized with respect to $dCCA7$, in order to account for CCA geometry inter-variability.

The Python script used to calculate the adjacency matrix A and the CNs metrics is provided in the electronic supplementary material.

III. Results

A. CNs "all-to-all" analysis - Axial Velocity

A picture of the axial flow in the CB is presented in Fig. 4, where cycle-average V_{ax} volumetric maps of are displayed. Regions with predominant unidirectional flow (i.e., the CCA) are characterized by high positive values of cycle-average V_{ax}. On the contrary, the predominant negative axial velocity characterizing the flow at the carotid bulb highlights the presence of flow reversal in that region.

For each investigated CB model, the probability density function (PDF) of the correlation coefficients R_{ij}^V between all pairs of nodal V_{ax} time-histories is presented in Fig. 5. In general, all PDFs present a peak on the right and a tail on the left side (i.e., the PDFs are left-skewed, as quantified by the negative skewness values in Table II in the Appendix). The probability associated with negative correlation between V_{ax} time-histories is not negligible, indicating the presence of flow reversal with respect to the main flow direction (i.e., along the centerline from CCA to ICA and ECA).

The volumetric maps of the normalized degree centrality DC (Fig. 5) highlight that in general axial velocity time-histories in CCA nodes present high DC values, while nodes located at the outer wall of the carotid bulb present low DC values, indicating that dynamically-distinct regions can be identified: (1) regions where forward flow dominates, in particular in the proximal CCA, in which the nearest neighborhoods of the V_{ax} time-histories are a large fraction (high DC) of the nodes of the network, or, in other words, V_{ax} time-histories are correlated beyond threshold with a large fraction of the axial velocities characterizing CB hemodynamics; (2) regions where flow is slow, recirculating, with direction reversal, in particular close to the outer wall of the carotid bulb where these flow features are associated to propensity to plaque formation and progression [4], [40]. In the latter regions the nearest neighborhoods of V_{ax} time-histories are a small fraction (low DC) of the nodes of the network.

The distribution of V_{ax} time-histories average nearest neighbors normalized degree centrality values *vs.* DC, $\langle DC_{nn}|DC\rangle$, is presented in Fig. 16 in the Appendix. In general, all the investigated models exhibit a markedly assortative behavior of the network, highlighted by $\langle DC_{nn}|DC\rangle$ trend, increasing function of *DC*, in the range of low DC values (i.e., for DC < 40%, in most of the cases). At higher DC values, $\langle DC_{nn}|DC\rangle$ presents a plateau, suggesting that the nearest neighbors of highly-connected nodes are all connected to a similar fraction of nodes inside the bifurcation model. The assortativity of the network, more evident at small and medium DC values, is further confirmed by the positive values of the assortativity coefficient *r* for each of the ten V_{ax}-based networks (Table II in the Appendix).

In terms of topological dispersion of the V_{ax}-based networks, measured using the average shortest path length (a physical interpretation for $ASPL$ is given in Table I), it emerges that two generic nodes are separated by a 1.53-links path, on average

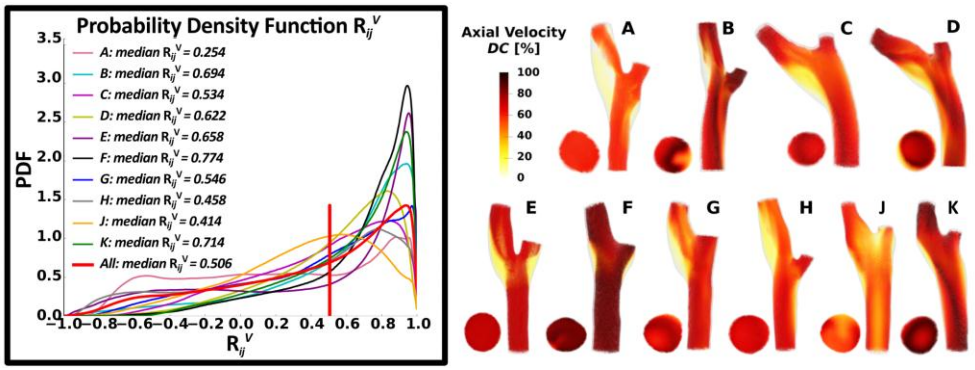

Fig. 5. Volumetric maps of DC for the ten *"all-to-all"* V_{ax}-based networks. For each model the CCA7 cross-sectional views are also displayed. The PDFs of the correlation coefficients R_{ij}^V between all pairs of V_{ax} time-histories are also presented in the black box. The median value (0.506) of the overall distribution obtained by pooling together the R_{ij}^V of all ten CB models (red curve) was set as threshold $\hat{R}^V$ to build the V_{ax}-based networks.

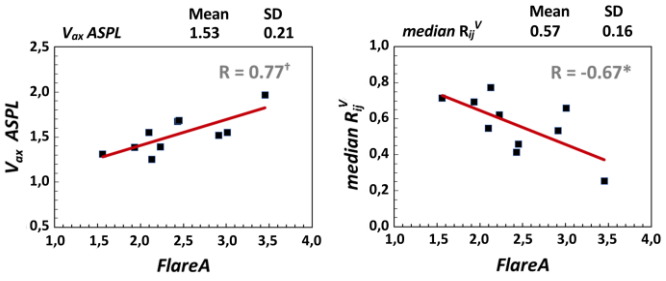

Fig. 6. *"All-to-all"* V_{ax} CNs. Association between the geometric descriptor *FlareA* and: the topological metric *ASPL* (left panel); the median value of R_{ij}^V coefficients (right panel). A significant positive correlation emerges between *FlareA* and *ASPL*, indicating the effect of the bifurcation expansion in disrupting links between the nodes, as also corroborated by the negative trend observed between *FlareA* and the median value of R_{ij}^V (*$p_{value} < 0.05$; †$p_{value} < 0.01$).

(*ASPL* range: 1.25-1.97). The association between the topological distance between two nodes and the expansion at the bifurcation can be appreciated in the scatter plot of *ASPL vs.* geometric descriptor *FlareA* (Fig. 6). The *ASPL* of V_{ax}-based networks and *FlareA* are positively correlated (R = 0.77, $p < 0.01$), implying that the expansion at the bifurcation significantly contributes to break up the topological links of the network and is therefore a putative mechanism of correlation dispersion of axial velocity time-histories. Fig. 6 also highlights the emergence of a negative correlation (R = -0.67, $p < 0.05$) between *FlareA* and the median value of R_{ij}^V (values of the latter quantity are listed in the inset of Fig. 5). This implies that when *FlareA* is larger, R_{ij}^V is generally lower, and the V_{ax}-based CN has fewer links (since it is smaller the area under the PDF for $R_{ij}^V > \widehat{R}^V$), thus requiring, on average, a longer path (measured by *ASPL*) connecting node couples. In a larger bifurcation expansion, V_{ax} time-histories become topologically more isolated, and a longer path is necessary to connect them in those vascular territories where the geometry does not divert the flow from the axial direction. This topological separation induced by the CB flare seems to reflect also a physical separation, as evidenced by the visual inspection of the volumetric maps of metric *AED* (Fig. 7), quantifying the Euclidean length of persistence of the correlation in the V_{ax}-based networks. In detail, it emerges from *AED* maps that V_{ax} time-histories located close to CCA7 and ICA5 sections are characterized by a neighborhood that expands on an anatomical distance equivalent to 3 CCA7 diameters or more, confirming the persistence of correlated V_{ax} structures in those regions. However, lower *AED* values characterize nodes located close to the outer wall of the carotid bulb. The V_{ax} time-histories in that region, typically characterized by flow reversal (i.e., negative axial velocity values), present an *AED* quantifiable in one CCA7 diameter (Fig. 7).

B. CNs "one-to-all" analysis – Inlet flow rate vs. Axial Velocity

The influence that the personalized inlet flow rate time-history Q has on V_{ax}, evaluated in terms of correlation R_i^Q, can be appreciated in Fig. 8, where the map of correlation values above the median ($\widehat{R}_i^Q = 0.79$) of the PDF distribution pooled over the ten models are displayed. Fig. 8 highlights that, in general, the highest R_i^Q values are located in the proximal segment of the CCA, as expected. The cross-sectional views are characterized by variegated correlation patterns, since in general the CCA7 does not correspond to the inlet section where the inflow boundary condition Q was applied (Fig. 1). High correlation values are restored distally in the ICA and ECA, although with some inter-variability deriving from the patient-specific flow waveform shapes applied as flow boundary conditions in CFD simulations [27]. Lower correlation with Q characterizes V_{ax} time-histories in the proximal ICA and in the carotid bulb. To quantify the anatomical length of persistence of the V_{ax}- Q correlation within each CB model, the *AWED* is reported in Fig. 8 and represented with a red line: it can be observed that the correlation between the inflow rate Q and V_{ax} time-histories keeps persistence around the distal CCA for some of the ten investigated cases (B, C, D, F, K), while in the remaining models the correlation expires within a shorter distance (below 1.88 *dCCA7*). A negative, almost significant trend (R = -0.59, $p = 0.07$) emerges between *AWED* and *FlareA* (Fig. 8), i.e., the average distance

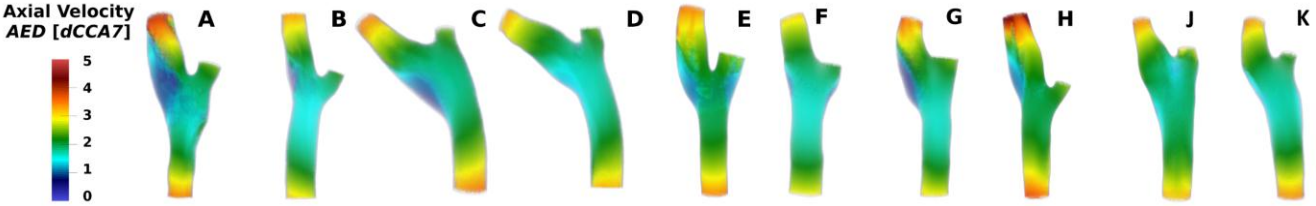

Fig. 7. *"All-to-all"* V_{ax} CNs. Volumetric maps of *AED*, i.e., the Euclidean length of persistence of correlated V_{ax} structures in the CB. *AED* is measured in terms of CCA7 diameters (*dCCA7*), in order to account for CCA geometry inter-variability. Low *AED* values (below 1 *dCCA7*) at the carotid bulb reflect the impact of the bifurcation expansion in reducing the sphere of influence of axial flow in that region.

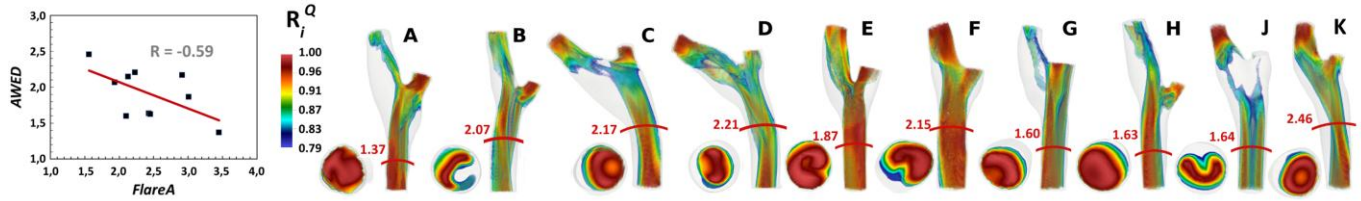

Fig. 8. Volumetric maps of the correlation R_i^Q between V_{ax} time-histories and the personalized inlet flow rate (Q) waveform in the *"one-to-all"* CNs. Volumetric maps show only V_{ax} *vs.* Q correlations above the median value (0.79) of the R_i^Q PDF distribution pooled over the ten models. For each model the CCA7 cross-sectional views are also displayed. The average Euclidean length of persistence of the V_{ax} *vs.* Q correlation (*AWED*) is indicated on each CB model by a red line in terms of CCA7 diameters. The scatter plot on the left indicates a negative, almost significant trend between *AWED* and *FlareA*.

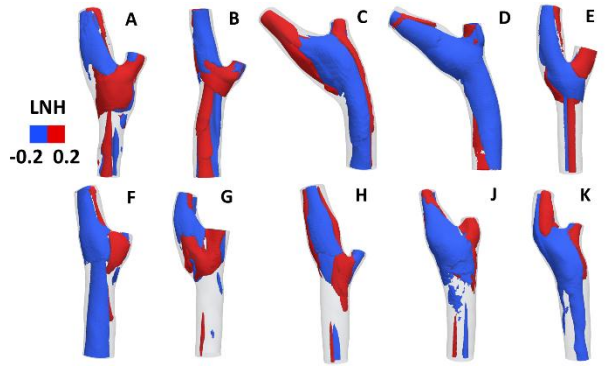

Fig. 9. Volumetric representation of the helical flow in the CB models as given by the visualization of cycle-average LNH isosurfaces. Negative (positive) LNH values identify left-handed (right-handed) counter-rotating helical structures.

of correlation between V_{ax} time-histories and the inlet volume flow rate waveform decreases as the expansion at the bifurcation increases.

C. CNs "all-to-all" analysis – Kinetic Helicity Density

A visualization of the bihelical, counter-rotating blood flow patterns in the investigated CB models is presented in Fig. 9. The PDFs of the correlation coefficients R_{ij}^H between all pairs of H_k time-histories are presented in Fig. 10. A feature common to all the CBs is that the R_{ij}^H PDF is markedly symmetric around zero (Table II in the Appendix). Such a symmetry is the quantitative confirmation that distinguishable counter-rotating helical flow patterns (characterized by H_k time-histories opposite in sign along the cardiac cycle) mark out the CB hemodynamics, consistent with previous observations [6], [9], [25]. For a more in-depth analysis, the PDFs of R_{ij}^H obtained by separating the CCA segment (from CCA7 to CCA3) from the bifurcation (BIF) region are analyzed (Fig. 10). From the comparison, it emerges that in general, the PDFs of the R_{ij}^H in the BIF region present a peak around zero correlation, while in the CCA the R_{ij}^H distributions tend to be bimodal, with the two maxima close to the extreme correlation values (i.e., -1 and 1) suggesting that the presence of strongly correlated and anti-correlated H_k time-histories is highly probable in the CCA. This correlation distribution subtends the existence of two distinguishable counter-rotating helical flow structures transported in the CCA along the cardiac cycle. On the opposite, the bifurcation tends to weaken the correlation of the H_k time-histories. This is quantitatively confirmed by the probability (i.e., the areas under the PDF curves in Fig. 10) of low ($|R_{ij}^H| \leq 0.2$) and high ($|R_{ij}^H| \geq 0.8$) correlation for H_k time-histories in CCA and in BIF (bar chart in Fig. 10): the scarcely correlated H_k time-histories are mainly located in the BIF region, the strongly correlated ones being located in the CCA.

The DC volumetric maps of H_k-based networks reflect the blood flow arrangement in helical counter-rotating structures (Fig. 11). In particular, it can be observed that positively correlated H_k time-histories form two clearly separated regions of low and high DC value, corresponding to those counter-rotating helical flow patterns conveyed from the CCA into the bifurcation [6], [9], [25]. The DC-based visualization of such intravascular flow features is enriched with the quantitative information provided by the DC metric. In particular, Fig. 11 clearly shows how positively correlated H_k time-histories give rise to connected networks in the CCA (as also evident from the cross-sectional views of the CCA7 sections in Fig. 11), and in the bifurcation. The negatively correlated H_k time-histories, reported in Fig. 17 in the Appendix, represent the complement of Fig. 11. As a consequence, DC measures the similarity between the dynamics of helical flow patterns, proving that large portions (i.e. high DC) of those distinguishable structures, usually visualized and described in terms of integral quantities [6], [9], exhibit also a similar time-dependent behavior.

From the analysis of the distributions of the H_k average nearest neighbors normalized degree centrality $\langle DC_{nn}|DC\rangle$ *vs.* DC (Fig. 18 in the Appendix) it emerges that, in general, the $\langle DC_{nn}|DC\rangle$ distribution has a sigmoid shape, with a steep positive slope in the range 45% < DC < 55%, where the assortative behavior of the networks is more pronounced. The assortativity of the H_k-based CNs is also proved by the positive values of the assortativity coefficients r (Table II in the Appendix) and reflects the tendency of H_k time-histories to connect to H_k time-histories with similar DC.

In terms of topological dispersion of the H_k-based networks, as measured by $ASPL$, two generic nodes are separated by a 1.49-links path on average ($ASPL$ range: 1.48-1.50) (Fig. 12). From the analysis of the average topological distance between nodes *vs.* the geometric expansion at the bifurcation ($ASPL$ vs. *FlareA*) reported in Fig. 12, no significant trend emerges (R = 0.57, p = 0.09). No association emerges also between *ASPL* and the median values of R_{ij}^H (R = -0.61, p = 0.06, Fig. 12), a consequence of the low dispersion of $ASPL$ and median R_{ij}^H values.

Finally, the AED volumetric maps for the H_k-based networks are presented in Fig. 13. H_k time-histories with the largest AED are located close to CCA7 and ICA5 sections, similarly to what observed for V_{ax} (Fig. 7). Helical flow patterns developing in those regions propagate maintaining correlation at an average anatomical distance of 3.5 CCA7 diameters or more. In the bifurcation region, helical structures exhibit lower AED values (from 1.5 to 2 CCA7 diameters).

IV. Discussion

Given the well-established key role played by intravascular flow in conditioning WSS and its physiological significance in terms of flow stability and mass transport, a plethora of cardiovascular fluid mechanics studies [10], [25], [34], [41]–[43] have provided a detailed analysis of fluid structures in the bulk of the vessels. However, most studies, in particular the ones focusing on the association of hemodynamic risk with vascular disease, tend to apply a "reductionist" approach, in mathematical terms (mostly focused on cycle-average values). To further explain, such approach usually neglects the spatiotemporal evolution and the persistence length of correlated blood flow patterns as a whole in the vasculature. This is mostly motivated by the clinical need of synthetizing the complexity of four-dimensional phenomena, with the risk of an information loss that (at least partially) limits the collective emergence of hemodynamic phenotypes with marked potential in terms of (1) basic comprehension of the physiopathology of the vasculature, and of (2) diagnostics/prognostics application.

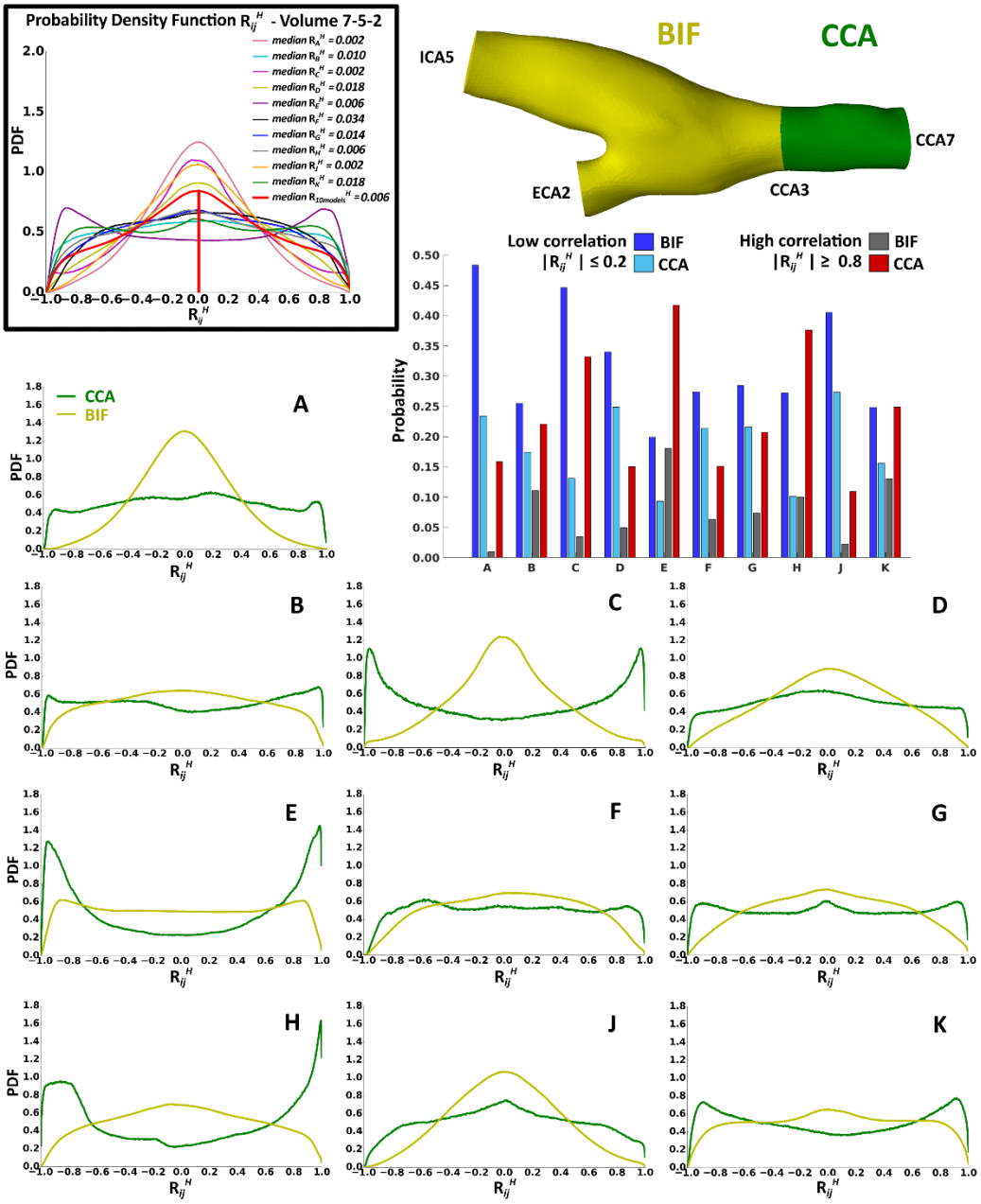

Fig. 10. PDFs of the correlation R_{ij}^H between H_k time-histories in the CB models (back box). The PDFs distributions are all almost symmetric around zero, quantitatively confirming the presence of the two distinguishable counter-rotating helical structures as a characteristic feature of the CB hemodynamics. For each model the PDFs of the R_{ij}^H values obtained by separating the CCA segment from the BIF region are also displayed. The values of the area under the PDF curves indicating low ($|R_{ij}^H| \le 0.2$) and high ($|R_{ij}^H| \ge 0.8$) correlation probability for H_k time-histories in CCA and BIF are also displayed in the bar chart.

Fig. 11. Volumetric maps of *DC* for the ten *"all-to-all"* H_k-based networks. The CCA7 cross-sectional views highlight the existence of two clearly separated low and high *DC* regions, according to the existence of two distinguishable, counter-rotating, and dynamically correlated helical flow structures.

Here, we propose a method to investigate cardiovascular flows, exploring the potential of CNs when applied to patient-specific computational hemodynamics. In particular, the integrated approach is here applied to investigate the underlying structure and organization of computational hemodynamic flows in ten patient-specific models of human CB. To the best of our knowledge, the application of CNs to understand blood flow advection mechanisms in realistic cardiovascular flows has never been explored before. Thanks to the perspective offered by networks science, here correlated flow patterns are

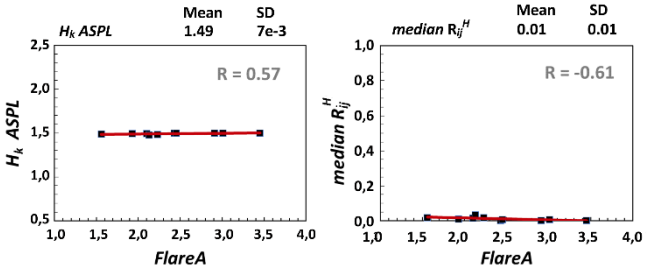

Fig. 12. *"All-to-all"* H_k CNs. Association between the geometric descriptor *FlareA* and: the topological metric *ASPL* (left panel); the median value of R_{ij}^H coefficients (right panel). The ranges of the vertical axes are consistent with Fig. 6, to underline that for H_k no significant association emerges between the investigated quantities. This indicates that the topological compactness of H_k networks is less sensitive to geometry than V_{ax} networks, in the CB.

unveiled, drawing upon the similarity between their dynamical processes, and the persistence length of fluid structures as they are conveyed into the CB is measured. To do that, the interdependence between hemodynamic time-histories defined in discrete computational domains is investigated by the so-called correlation networks [18]–[20], [22], [38], [44].

Associations, albeit not always significant, are also reported here between CNs metrics and a geometric indicator of disturbed flow. In particular, the bifurcation flare (i.e., the expansion) is considered here, because it has been reported that a large expansion at the bifurcation produces flow separation and in general flow disturbances promoting vascular disease (e.g., atherosclerosis [31], [45], or restenosis [46]). In this sense the findings of the study highlight the potential of CNs to quantify the impact of vascular geometry on the preservation/loss of similarity of flow patterns in the streaming blood, enforcing and widening the previously shown associations between CB geometry and hemodynamic disturbances [25], [31], [47]. With the application of the CNs formalism, the here proposed viewpoint on cardiovascular flows is able to highlight their arrangement in "functionally" connected patterns, encoding spatiotemporal similarity along the cardiac cycle and measuring both its topological and anatomical length of persistence. In doing that, we aim to contribute to give a less elusive definition of "coherent hemodynamic structures" as structures which are easily recognizable because they undergo similar dynamical evolution along the cardiac cycle and persist in space.

A. *Hemodynamic interpretation of the CNs-based analysis*

An interpretation of the organization principles behind CB hemodynamics is given by characterizing the structure of the networks (Table I), in which the spatiotemporal evolution along the cardiac cycle of correlated intravascular flow patterns is encapsulated.

The determination of the topological "centrality" of a node inside a network, as given by metric DC, allows both the identification and visualization of dynamically-similar hemodynamic features. As for V_{ax}, a correlated axial flow (high DC) develops mainly in the CCA, while the outer wall of the carotid bulb emerges as the more topologically isolated area, with very low DC (Fig. 5), reflecting the presence of a recirculation region with more intricate, uncorrelated V_{ax} spatiotemporal patterns. On the other hand, H_k appears more spatiotemporally compact, in general characterized by the absence of relevant topologically isolated structures (DC always greater than 35%), and by symmetry in the correlated helical flow patterns (Fig. 11). These results differ from conventional visualizations of axial and helical flow maps (Fig. 4 and 9, respectively), which are unable to encode the spatiotemporal similarity of intravascular flow structures in a snapshot or in a distance function.

In this study, the use of networks preserving the spatial collocation of two-point correlations enabled the measurement of the anatomical "sphere of influence" of correlated intravascular flow quantities, through the computation of metric AED: in CCA and distal ICA, axial and helical flow exhibit a persistence length of correlation of around 3 CCA7 diameters (Fig. 7 and 13); in the bifurcation region, bulb expansion reduces the sphere of influence of correlated hemodynamic structures (low AED), indicating that such structures are not preserved on a long distance but are confined within the region around the bifurcation expansion. In the case of the CB this result, while confirming what can be arguably shown by other simpler hemodynamic analyses [9], for the first time measures to what extent flow similarity is disrupted by specific vascular geometric features.

B. *The different impact of bifurcation expansion on axial velocity and helical flow*

The influence of vascular geometry on the persistence length of intravascular flow patterns is discussed here (and summarized in Table I). The topological dispersion in the H_k-based networks, as measured by $ASPL$, is moderately lower than V_{ax}, and presents less inter-variability (Fig. 12 and 6, respectively). In addition, while for the case of the V_{ax}-based networks $ASPL$ is positively correlated with *FlareA* (R = 0.77, $p < 0.01$, Fig. 6), no significant association emerges for the H_k-based networks (R = 0.57, $p = 0.09$, Fig. 12). In other terms, the H_k-based networks are less sensitive to geometry than the V_{ax}-based networks, as $ASPL$ for the H_k-based networks is not sensitive to the inter-variability in *FlareA*. This leads to presume a different action of the bulb expansion on the two intravascular quantities: a larger expansion, by inducing flow separation at the outer wall, disrupts correlation of axial velocity time-histories more than helical flow structures

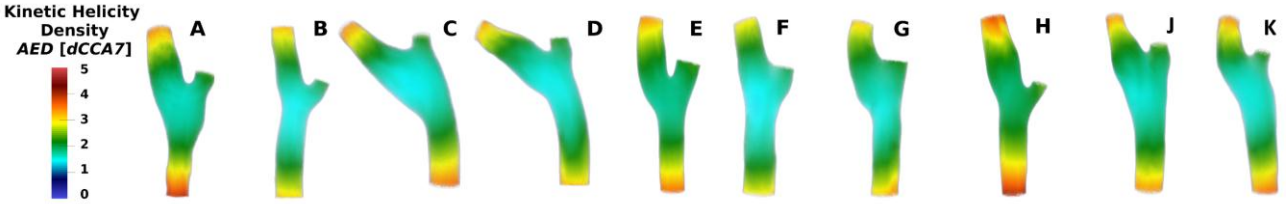

Fig. 13. *"All-to-all"* H_k CNs. Volumetric maps of AED, i.e., the Euclidean length of persistence of correlated H_k structures in the CB. AED is measured in terms of CCA7 diameters ($dCCA7$), in order to account for CCA geometry inter-variability. At the carotid bulb, correlated helical flow structures still persist over 1.5 $dCCA7$, thus proving the less disruptive effect of the bifurcation expansion on the connections between H_k time-histories.

TABLE I
SUMMARY OF THE HEMODYNAMIC INTERPRETATION OF THE COMPLEX NETWORKS (CNS) TOPOLOGICAL ANALYSIS AND IMPLICATIONS FOR V_{ax} AND H_k

Topological CNs metric	Hemodynamic interpretation	Implications for V_{ax}	Implications for H_k
		"*all-to-all*" analysis	
DC	Dynamic similarity between hemodynamic patterns	- high DC in the CCA (forward flow) - low DC in the carotid bulb (recirculating/reversed flow)	two clearly separated regions of low and high DC value suggest the existence of two distinguishable, counter-rotating, dynamically correlated, helical flow patterns
$ASPL$	Functional compactness/dispersion of hemodynamic structures	connections in axial flow sensitive to CB flare, which causes correlation dispersion	connections in helical flow: - overall compact (low mean $ASPL$) and stable (low SD) - less sensitive to the CB flare
AED	Persistence length of correlation of hemodynamic structures	correlated V_{ax} structures: - persist for 3 $dCCA7$ in CCA and distal ICA - expire in 1 $dCCA7$ in CB flare	correlated H_k structures: - persist for 3 $dCCA7$ in CCA and distal ICA - persist over 1.5 $dCCA7$ in CB flare
		"*one-to-all*" analysis	
$AWED$	Persistence length of correlation between V_{ax} and inflow rate Q	length of V_{ax} *vs.* Q correlation: - generally persists up to distal CCA - decreases in larger CB flares	-

transported through the CCA into the carotid bulb [6]. This presumption is corroborated, in the V_{ax}-based networks, by the low DC and AED values (discussed in Section III-A) in the recirculation region of the bulb (Fig. 5 and 7), which imply: (1) a topological separation of the nodes in that region from the rest of the network (thus highlighting the presence of two dynamically-distinct regions); (2) a dynamic similarity among the nodes of each region.

Furthermore, the AED values in the bifurcation region, higher in the H_k-based network (from 1.5 to 2.0 CCA7 diameters, Fig. 13) than V_{ax} (around 1.0 CCA7 diameters, Fig. 7): (1) confirm the effect of the carotid bulb in preserving the topological connection between helical flow structures more than axial velocity patterns; (2) prove that the impact of the bifurcation expansion on flow topology can be quantified in terms of persistence length within the fluid domain.

C. Insights from the "one-to-all" analysis

The *"one-to-all"* analysis here introduced allows the calculation of the anatomical "sphere of influence" of the subject-specific inflow rate Q on the axial flow in the CB. This allows to estimate the length of correlation of the flow rate waveform driving perfusion along the main blood flow direction, imparted by, e.g., geometry (the bifurcation expansion in the case under study), downstream vascular impedance, wave reflection. Additionally, the disrupting effect of the CB geometric expansion on the V_{ax}-Q length of correlation is reflected by the negative association, albeit not significant (R = -0.59, p = 0.07), observed between the introduced metric $AWED$ and *FlareA* (Fig. 8).

V. CONCLUSION

In conclusion, the here presented CNs-based exploration of the spatiotemporal complexity of cardiovascular flows simulated using the paradigm of computational hemodynamics has led to the quantification of the persistence length of correlation of hemodynamic quantities in a dataset of personalized models of human carotid bifurcations. Our findings suggest that the geometry of the carotid bulb, in particular its expansion (already identified as the main determinant of disturbed shear [31], [47]), plays a major role in differently weakening/preserving spatiotemporal similarity in axial flow and in helical flow, by influencing the topological connections between fluid mechanics quantities.

The integrated CNs and computational hemodynamics approach allows the identification of fluid structures undergoing similar dynamical evolution. This opens avenues for further comprehension of the blood-vessel interaction physiopathology, in particular for those markedly "multidirectional" flow districts (like in heart and aneurysms) where disruption of flow coherence may have significant diagnostic/prognostic implications.

APPENDIX

PDF properties of R_{ij}^{V} and R_{ij}^{H} correlation coefficients, together with CNs assortativity are reported in Table II.

TABLE II
MEDIAN AND SKEWNESS VALUES OF R_{ij}^{V} AND R_{ij}^{H}, AND ASSORTATIVITY COEFFICIENT r FOR THE V_{ax}- AND H_k-BASED CNS

CB Model	V_{ax}-based networks			H_k-based networks		
	Median	Skewness	r	Median	Skewness	r
A	0.254	-0.204	0.683	0.002	0.027	0.265
B	0.694	-1.348	0.218	0.010	-0.007	0.627
C	0.534	-0.684	0.360	0.002	0.015	0.250
D	0.622	-0.961	0.237	0.018	-0.020	0.541
E	0.658	-0.782	0.779	0.006	-0.001	0.639
F	0.774	-1.387	0.418	0.034	-0.023	0.594
G	0.546	-0.748	0.382	0.014	-0.007	0.674
H	0.458	-0.672	0.529	0.006	0.024	0.588
J	0.414	-0.578	0.329	0.002	0.048	0.341
K	0.714	-1.029	0.147	0.018	-0.012	0.713
All models	0.506	-0.750	-	0.006	0.009	-

Each CB geometry was characterized using the geometric descriptor *FlareA*, a measure of the maximum expansion at the carotid bulb with respect to the CCA, as shown in Fig. 14.

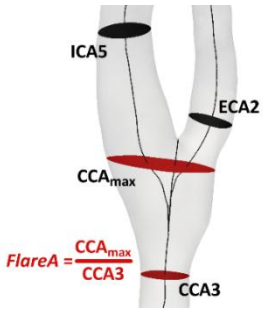

Fig. 14. CCA$_{max}$ and CCA3 sections, whose areas define *FlareA*, are shown in red. CCA$_{max}$ is orthogonal to the average of the ICA and ECA centerlines, also shown. CCA: common carotid artery; ICA: internal carotid artery; ECA: external carotid artery.

The sketch in Fig. 15 shows how the axial velocity V_{ax} was calculated: locally the velocity vector **V** is projected along the "axial direction", here intended as the direction aligned with the tangent to vessel's centerline [32].

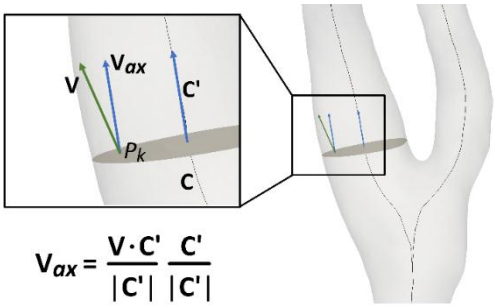

Fig. 15. Definition of axial velocity V_{ax} as the projection of the velocity vector **V** at the generic point $\boldsymbol{P_k}$ along the local vessel centerline **C**. **C'** is the vector tangent to the centerline, representing the local axial direction.

$\langle \mathrm{DC_{nn}}|\mathrm{DC}\rangle$ *vs.* DC curves for the *"all-to-all"* V_{ax} networks are reported in Fig. 16.

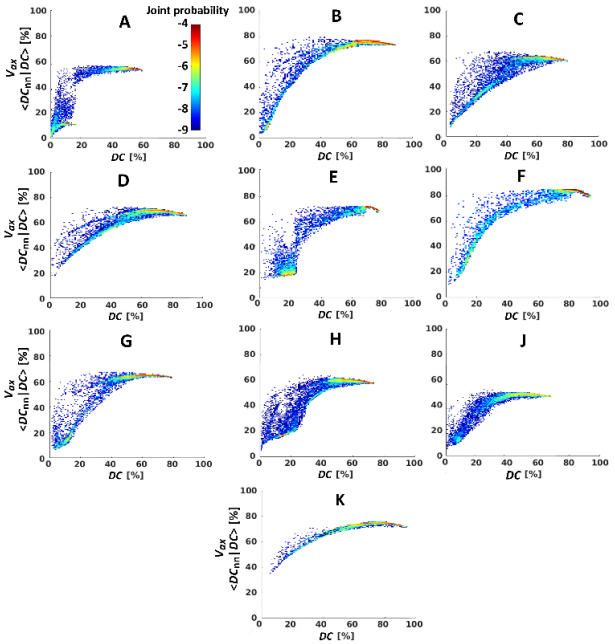

Fig. 16. Distribution of $\langle DC_{nn}|DC\rangle$ for the V_{ax} CNs. Colormap indicates the joint probability (in *ln* scale) for DC and $\langle DC_{nn}|DC\rangle$: higher joint probability values can be observed in the plateau region, at high values of DC.

"All-to-all" H_k CNs considering negatively correlated H_k time-histories were also built, in addition to the ones discussed in Section III-C and obtained from positively correlated H_k time-histories. As expected, the DC distributions of negatively (Fig. 17) and positively correlated (Fig. 11) H_k time-histories are exactly complementary.

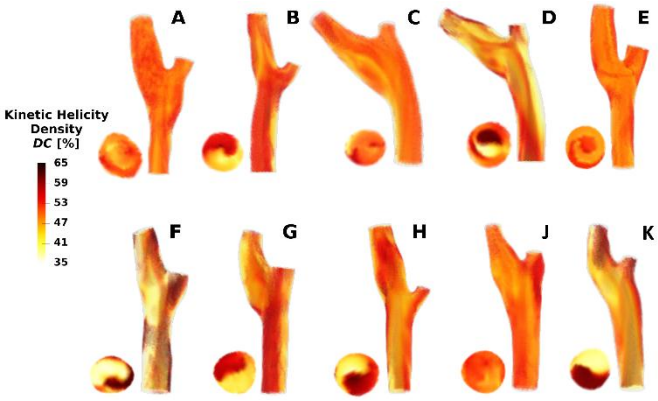

Fig. 17. Volumetric maps of DC for the ten *"all-to-all"* H_k-based networks built considering all the negatively correlated H_k time-histories (i.e., a link between nodes i and j exists ($A_{ij} = 1$) if $R^H_{ij} < 0$). The CCA7 cross-sectional views highlight two clearly separated low and high DC regions, perfectly complementary to the ones in Fig. 11 of Section III-C.

$\langle \mathrm{DC_{nn}}|\mathrm{DC}\rangle$ *vs.* DC curves for the *"all-to-all"* H_k networks are reported in Fig. 18.

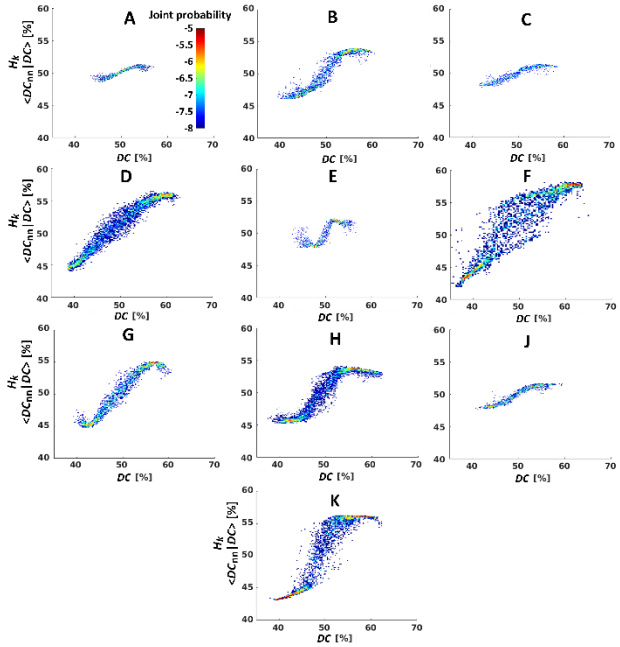

Fig. 18. Distribution of $\langle DC_{nn}|DC\rangle$ for the H_k CNs. Colormap indicates the joint probability (in *ln* scale) for DC and $\langle DC_{nn}|DC\rangle$: higher joint probability values can be observed in the plateau regions at extremes DC values, with the exception of model A where high values of joint probability are mainly located in the middle of the range of DC.

REFERENCES

[1] U. Morbiducci *et al.*, "Atherosclerosis at arterial bifurcations: evidence for the role of haemodynamics and geometry.," *Thromb. Haemost.*, vol. 115, pp. 484–492, Mar. 2016.

[2] Z. Stankovic *et al.*, "4D flow imaging with MRI.," *Cardiovasc. Diagn. Ther.*, vol. 4, pp. 173–192, Apr. 2014.

[3] C. A. Taylor and D. A. Steinman, "Image-Based Modeling of Blood Flow

and Vessel Wall Dynamics: Applications, Methods and Future Directions," *Ann. Biomed. Eng.*, vol. 38, pp. 1188–1203, 2010.

[4] D. N. Ku *et al.*, "Pulsatile flow and atherosclerosis in the human carotid bifurcation. Positive correlation between plaque location and low oscillating shear stress.," *Arteriosclerosis*, vol. 5, pp. 293–302, 1985.

[5] D. P. Giddens, C. K. Zarins, and S. Glagov, "The role of fluid mechanics in the localization and detection of atherosclerosis.," *J. Biomech. Eng.*, vol. 115, pp. 588–594, Nov. 1993.

[6] D. Gallo, D. A. Steinman, and U. Morbiducci, "An insight into the mechanistic role of the common carotid artery on the hemodynamics at the carotid bifurcation.," *Ann. Biomed. Eng.*, vol. 43, pp. 68–81, Jan. 2015.

[7] C. G. Caro *et al.*, "Secondary Flow in the Human Common Carotid Artery Imaged by MR Angiography," *J. Biomech. Eng.*, vol. 114, p. 147, Feb. 1992.

[8] P. J. Kilner *et al.*, "Helical and retrograde secondary flow patterns in the aortic arch studied by three-directional magnetic resonance velocity mapping.," *Circulation*, vol. 88, pp. 2235–2247, Nov. 1993.

[9] D. Gallo *et al.*, "Helical flow in carotid bifurcation as surrogate marker of exposure to disturbed shear.," *J. Biomech.*, vol. 45, pp. 2398–2404, Sep. 2012.

[10] P. A. Stonebridge *et al.*, "Spiral laminar flow in vivo.," *Clin. Sci. (Lond).*, vol. 91, pp. 17–21, Jul. 1996.

[11] U. Morbiducci *et al.*, "Mechanistic insight into the physiological relevance of helical blood flow in the human aorta. An in vivo study." *Biomech. Model. Mechanobiol*, vol. 10, pp. 339–355, 2011.

[12] U. Gulan *et al.*, "Experimental Investigation of the Influence of the Aortic Stiffness on Hemodynamics in the Ascending Aorta," *IEEE J. Biomed. Heal. Informatics*, vol. 18, pp. 1775–1780, Nov. 2014.

[13] S. Boccaletti *et al.*, "Complex networks: Structure and dynamics," *Phys. Rep.*, vol. 424, pp. 175–308, 2006.

[14] J. Sun et al., "Complex Network Construction of Multivariate Time Series Using Information Geometry," *IEEE Trans. Syst. Man, Cybern. Syst.*, vol. 49, pp. 107–122, 2019.

[15] S. Havlin *et al.*, "Challenges in network science: Applications to infrastructures, climate, social systems and economics," *Eur. Phys. J. Spec. Top.*, vol. 214, pp. 273–293, 2012.

[16] S. Wang, W. Cheng, and G. Mei, "Efficient Method for Improving the Spreading Efficiency in Small-World Networks and Assortative Scale-Free Networks," *IEEE Access*, vol. 7, pp. 46122–46134, 2019.

[17] S. Mostafi *et al.*, "An Algorithm for Mapping a Traffic Domain Into a Complex Network: A Social Internet of Things Approach," *IEEE Access*, vol. 7, pp. 40925–40940, 2019.

[18] R. V Donner, E. Hernández-García, and E. Ser-Giacomi, "Introduction to Focus Issue: Complex network perspectives on flow systems," *Chaos An Interdiscip. J. Nonlinear Sci.*, vol. 27, p. 035601, Mar. 2017.

[19] J. F. Donges *et al.*, "Complex networks in climate dynamics," *Eur. Phys. J. Spec. Top.*, vol. 174, pp. 157–179, 2009.

[20] S. Scarsoglio, F. Laio, and L. Ridolfi, "Climate dynamics: a network-based approach for the analysis of global precipitation," *PLoS One*, vol. 8, p. e71129, 2013.

[21] K. Taira, A. G. Nair, and S. L. Brunton, "Network structure of two-dimensional decaying isotropic turbulence," *J. Fluid Mech.*, vol. 795, 2016.

[22] S. Scarsoglio, G. Iacobello, and L. Ridolfi, "Complex networks unveiling spatial patterns in turbulence," *Int. J. Bifurc. Chaos*, vol. 26, p. 1650223, 2016.

[23] C. Liu, W.-X. Zhou, and W.-K. Yuan, "Statistical properties of visibility graph of energy dissipation rates in three-dimensional fully-developed turbulence," *Phys. A Stat. Mech. its Appl.*, vol. 389, pp. 2675–2681, 2010.

[24] G. Iacobello *et al.*, "Spatial characterization of turbulent channel flow via complex networks.," *Phys. Rev. E*, vol. 98, p. 13107, Jul. 2018.

[25] D. Gallo et al., "Segment-specific associations between local haemodynamic and imaging markers of early atherosclerosis at the carotid artery: an in vivo human study," *J. R. Soc. Interface*, vol. 15, p. 20180352, Oct. 2018.

[26] J. Martorell *et al.*, "Extent of flow recirculation governs expression of atherosclerotic and thrombotic biomarkers in arterial bifurcations," *Cardiovasc. Res.*, vol. 103, pp. 37–46, Jul. 2014.

[27] Y. Hoi *et al.*, "Effect of common carotid artery inlet length on normal carotid bifurcation hemodynamics.," *J. Biomech. Eng.*, vol. 132, p. 121008, Dec. 2010.

[28] P. D. Minev and C. Ross Ethier, "A characteristic/finite element algorithm for the 3-D Navier–Stokes equations using unstructured grids," *Comput. Methods Appl. Mech. Eng.*, vol. 178, pp. 39–50, Jul. 1999.

[29] L. Antiga *et al.*, "An image-based modeling framework for patient-specific computational hemodynamics," *Med. Biol. Eng. Comput.*, vol. 46, p. 1097, 2008.

[30] J. B. Thomas *et al.*, "Variation in the carotid bifurcation geometry of young versus older adults: implications for geometric risk of atherosclerosis.," *Stroke*, vol. 36, pp. 2450–2456, Nov. 2005.

[31] P. B. Bijari *et al.*, "Improved prediction of disturbed flow via hemodynamically-inspired geometric variables.," *J. Biomech.*, vol. 45, pp. 1632–1637, Jun. 2012.

[32] U. Morbiducci *et al.*, "A rational approach to defining principal axes of multidirectional wall shear stress in realistic vascular geometries, with application to the study of the influence of helical flow on wall shear stress directionality in aorta.," *J. Biomech.*, vol. 48, pp. 899–906, Apr. 2015.

[33] A. Frydrychowicz et al., "Visualization of iliac and proximal femoral artery hemodynamics using time-resolved 3D phase contrast MRI at 3T.," *J. Magn. Reson. Imaging*, vol. 25, pp. 1085–1092, May 2007.

[34] U. Morbiducci *et al.*, "Helical flow as fluid dynamic signature for atherogenesis risk in aortocoronary bypass. A numeric study.," *J. Biomech.*, vol. 40, pp. 519–534, 2007.

[35] X. Liu *et al.*, "Physiological significance of helical flow in the arterial system and its potential clinical applications.," *Ann. Biomed. Eng.*, vol. 43, pp. 3–15, Jan. 2015.

[36] P. A. Stonebridge *et al.*, "Spiral Laminar Flow: a Survey of a Three-Dimensional Arterial Flow Pattern in a Group of Volunteers.," *Eur. J. Vasc. Endovasc. Surg.*, vol. 52, pp. 674–680, Nov. 2016.

[37] H. K. Moffatt and A. Tsinober, "Helicity in Laminar and Turbulent Flow," *Annu. Rev. Fluid Mech.*, vol. 24, pp. 281–312, Jan. 1992.

[38] R. V Donner *et al.*, "Recurrence-based time series analysis by means of complex network methods.," *Int. J. Bifurc. Chaos*, vol. 21, pp. 1019–1046, Apr. 2011.

[39] M. E. J. Newman, "Assortative Mixing in Networks," *Phys. Rev. Lett.*, vol. 89, p. 208701, Oct. 2002.

[40] C. K. Zarins et al., "Carotid bifurcation atherosclerosis. Quantitative correlation of plaque localization with flow velocity profiles and wall shear stress.," *Circ. Res.*, vol. 53, pp. 502–514, Oct. 1983.

[41] X. Liu, Y. Fan, and X. Deng, "Effect of spiral flow on the transport of oxygen in the aorta: a numerical study.," *Ann. Biomed. Eng.*, vol. 38, pp. 917–926, Mar. 2010.

[42] J. Garcia *et al.*, "Volumetric quantification of absolute local normalized helicity in patients with bicuspid aortic valve and aortic dilatation.," *Magn. Reson. Med.*, vol. 78, pp. 689–701, Aug. 2017.

[43] G. De Nisco *et al.*, "The Atheroprotective Nature of Helical Flow in Coronary Arteries," *Ann. Biomed. Eng.*, vol. 47, pp. 425–438, Feb. 2019.

[44] S. Scarsoglio, F. Cazzato, and L. Ridolfi, "From time-series to complex networks: Application to the cerebrovascular flow patterns in atrial fibrillation.," *Chaos*, vol. 27, p. 93107, Sep. 2017.

[45] P. B. Bijari, B. A. Wasserman, and D. A. Steinman, "Carotid bifurcation geometry is an independent predictor of early wall thickening at the carotid bulb," *Stroke*, vol. 45, pp. 473–478, Feb. 2014.

[46] M. Domanin *et al.*, "Prediction of Long Term Restenosis Risk After Surgery in the Carotid Bifurcation by Hemodynamic and Geometric Analysis," *Ann. Biomed. Eng.*, vol. 47, pp. 1129–1140, 2019.

[47] S.-W. Lee *et al.*, "Geometry of the carotid bifurcation predicts its exposure to disturbed flow.," *Stroke*, vol. 39, pp. 2341–2347, Aug. 2008.